Ion-beam processing of silicon at keV energies: A molecular-dynamics study

M.-J. Caturla,* T. Díaz de la Rubia,† and L. A. Marqués
Lawrence Livermore National Laboratory, University of California, Livermore, California 94550

G. H. Gilmer
Bell Laboratories, Murray Hill, New Jersey 07974
(Received 7 May 1996)

We discuss molecular-dynamics simulations of ion damage in silicon, with emphasis on the effects of ion mass and energy. We employ the Stillinger-Weber potential for silicon, suitably modified to account for high-energy collisions between dopant-silicon and silicon-silicon pairs. The computational cells contain up to 10^6 atoms and these are bombarded by B and As atoms at incident energies from 1 keV up to 15 keV. We show that the displacement cascade results in the production of amorphous pockets as well as isolated point defects and small clusters with populations which have a strong dependence on ion mass and a weaker relationship to the ion energy. We show that the total number of displaced atoms agrees with the predictions of binary collision calculations for low-mass ions, but is a factor of 2 larger for heavy-ion masses. We compare the simulations to experiments and show that our results provide a clear and consistent physical picture of damage production in silicon under ion bombardment. We studied the stability of the damage produced by heavy ions at different temperatures and the nature of the recrystallization mechanism. The inhomogeneous nature of the damage makes the characterization of the process through a single activation energy very difficult. An *effective* activation energy is found depending on the pocket size. We discuss our results considering the Spaepen-Turnbull recrystallization model for an amorphous-crystalline planar interface.
[S0163-1829(96)09248-X]

I. INTRODUCTION

Silicon ion beam processing has long been a topic of considerable scientific and technological interest. From a fundamental viewpoint, the ion-solid interaction leads to defect production and free energy changes and, ultimately, at sufficiently high doses, to a crystal-to-amorphous (c-a) transformation of the irradiated silicon lattice.[1] This transformation is critically dependent on the irradiation parameters[2] and is controlled by a competition between damage accumulation and dynamic annealing.[3–5] The mass of the irradiating ion species,[2,6] the temperature of the substrate,[3,5] and the dose[3,7] and dose rate[3–5] of the irradiation all play an interdependent role. From a technological point of view, ion implantation followed by high-temperature annealing is a standard processing step in the manufacturing of silicon very large scale integrated (VLSI) devices.[8] Even at the low ion doses used in some manufacturing steps, implantation introduces disorder and defects into the lattice. Upon annealing, these defects interact with the dopant atoms and induce transient-enhanced diffusion (TED) of the dopant over long distances.[9–16] Also, at sufficiently high ion energy and dose interstitials may coalesce into extended defects (e.g., dislocation loops[9] and {311} defects[10]) and eventually, as these evaporate, dopant transport over long distances can also occur.[11] Understanding and controlling the deleterious phenomenon of TED has been identified as a critical issue in the development of future generations of semiconductor devices.[17]

Although much research has been devoted over the years to these subjects, questions remain as to the fundamental mechanisms of damage production during silicon-ion-beam processing. In particular, understanding and being able to predict the detailed nature and three-dimensional (3D) distribution of the damage induced in silicon by an ion beam is critical to the development of atomistic models of silicon processing for device manufacturing. This includes not only the defect production mechanisms themselves, but also the long-time evolution of the damage and the physical mechanisms of defect accumulation and phase transformation. For example, while some models[18] invoke an amorphization mechanism based on point defect accumulation, others employ a damage accumulation and amorphization mechanism based on the overlap of intracascade-produced amorphous zones.[19] However, no single model appears to properly account for all the experimental observations. For example, none of these models takes into account the dynamic annealing process that results in experimentally observed strong dose rate effects.[1,3–5]

At the most fundamental level, the study of ion-beam processing of semiconductors requires that the displacement cascades generated along the path of an energetic beam be well understood. Such cascades have been the subject of intense study for many years.[20] However, their small size ($\sim 10^{-25}$ cm^3) and short lifetime ($\sim 10^{-11}$ s) make their investigation by experimental means very difficult; only indirectly can the primary state of damage, that is, the source term for subsequent diffusion, be inferred.

Damage produced by implantation can be described in general terms by defining the number of displaced atoms (or Frenkel pairs) along the track of the incoming ion. Computer simulation codes such as TRIM (Ref. 21), and MARLOWE (Ref. 22), as well as analytical descriptions based on linear Boltzmann transport theory,[23] have generally been used for this purpose. These methods are all based on the binary col-

 © 1996 The American Physical Society

lision approximation (BCA).[24] Within this approximation, the collisions between recoils in the ion-induced displacement cascade occur only between moving and stationary atoms. Under such conditions, only collisions with energies higher than about 200 eV can be accurately treated. This approximation has as its most important consequence the fact that all low-energy solid-state or many-body effects on the dynamics of the displacement cascade are lost.

Recently, Jaraíz *et al.*[25] coupled a MARLOWE simulation of 40 keV Si implantation into Si at a dose of 5×10^{13} ions/cm^2 to a simple kinetic Monte Carlo simulation of point defect diffusion. In this treatment, the implantation damage is represented as vacancies, interstitials, or clusters of these point defects, but amorphous pockets are not included as distinct entities. The results clearly showed that for 40 keV Si, at a dose of 5×10^{13} cm^{-2}, bulk recombination of vacancies and interstitials dominates and the interstitial corresponding to the extra implanted ion makes the primary contribution to long-range diffusion. However, in order to develop more general models of damage accumulation and annealing, more accurate and physically correct descriptions of the as-implanted damage state and its evolution are required.

Molecular-dynamics (MD) simulation methods can be used to treat the full dynamics of the collision process.[26–28] MD is based on a simple integration of the classical equations of motion of an ensemble of atoms in a crystallite.[29] Because atom trajectories are computed from forces derived from the gradient of an interatomic potential and integrated using Newton's equations, the simulation can describe the complete phase space available to the system. Therefore, MD can help predict the formation of realistic damage microstructures not accessible to BCA-based calculations. In this paper, we present MD simulation results for boron- and arsenic-induced displacement cascades in silicon at energies expected for sub-0.25-μm complementary metal-oxide semiconductor (CMOS) technology, i.e., from 1 keV B to 15 keV As. We first outline the details of the simulation method and point out the major features of the Stillinger-Weber (SW) interatomic potential used to describe Si-Si interactions.[30] We compare B and As cases where either the range of the implanted ion or the damage energy deposited into the crystal is the same for both ions. The results are analyzed by studying the number and cluster size distribution of displaced atoms in the cascades. In the next section, we discuss the stability of these clusters, which is critical to understanding the dynamics of damage accumulation in silicon, as well as their local structure. We show that for As cascades the large disordered zones are indeed amorphous pockets of material. It is shown that large amorphous pockets are stable up to room temperature, but anneal out over periods of several hundred picoseconds at temperatures above 500 K. For B cascades, the clusters are small and can be described as actual agglomerations of small numbers of vacancies and interstitials. We compare the results to recent experimental observations and discuss their implications for the development of models of damage accumulation, extended defect formation, amorphization, and annealing. We conclude by outlining future calculations linking these MD simulations to models of defect transport over long length and time scales.

II. MOLECULAR-DYNAMICS SIMULATION

The MD simulations of ion-beam processing at keV energies discussed here employs computational crystals with up to 10^6 atoms, which correspond to a cube of silicon 271 Å on a side. Periodic boundary conditions are applied in the $\langle 100\rangle$ and $\langle 010\rangle$ directions, with a free surface at the topmost (001) plane. The bottom (001) plane is held fixed and a thermostat is implemented by coupling the atoms in the next four (001) planes to a thermal reservoir at constant temperature. After equilibration of the system, one atom [the primary knock-on atom (PKA)] is given the velocity corresponding to the implantation energy and beam angle of incidence that needs to be simulated. The ion trajectory and that of all subsequent secondary and higher order recoils are followed without any limitations as to which atoms are set into motion by the collisions. The simulation proceeds until the displacement cascade region reaches equilibrium with the surrounding thermal bath, that is, until all deposited energy has dissipated into the boundary and thermal reservoirs. Because of the large amount of energy deposited by the incident beam in the simulations, care must be taken to prevent energy from reentering the simulation box through the periodic boundaries. This is achieved by the application of damping to a layer of atoms in the atomic planes adjacent to the boundaries. The damping coefficient is chosen to ensure that energy arriving at the boundary is dissipated in the same manner as if the computational cell were surrounded by a much larger one, thus simulating the effect of an outside elastic continuum.[31,32]

In order to simulate ion-beam processes at nonzero temperatures, the simulation cell must be kept at constant temperature through the application of a constant temperature algorithm. We employ the Langevin equation of motion,[33] but apply it only to the atoms at and near the cell boundaries. Application of such temperature control algorithms permits simulations of high-temperature damage annealing to be performed with MD for periods of time long enough to dissolve the locally amorphous damage microstructure in silicon into groups of point defects.

In addition to temperature control, inelastic energy losses, which in some cases can be as important as elastic energy loss processes, must be taken into account. For the irradiation conditions described in this paper, inelastic energy losses to the electronic system do not lead to atomic displacements, but serve to dissipate energy away from the incoming ion and subsequent recoils. We describe this process by implementing a simple Lindhard electronic stopping power model.[34] In this model, valid for low-energy ions and recoils, the losses are described as a simple drag force applied as a damping of atomic velocities. Thus, the classical equations of motion are modified as

$$\mathbf{F}=m_i\ddot{x}_i-\beta\dot{x}_i\,, \tag{1}$$

where β is given by the Lindhard theory as

$$\beta=\frac{KNZ_1^{7/6}Z_2}{(Z_1^{2/3}+Z_2^{2/3})^{3/2}}, \tag{2}$$

where Z_1 is the atomic number of the projectile, Z_2 the atomic number of the target, $K=0.857$ (eV$^{1/2}$ Å^2), and N is

the target density. The electronic energy loss is assumed to be significant only for atoms with kinetic energies well above the initial thermal distribution in the crystal, and for this reason this damping term is applied only to atoms with kinetic energies above 1 eV. Since Langevin dynamics is applied to the atoms in the boundary of the box, the final equation that must be integrated to describe the dynamics of energetic atoms in these regions is

$$\mathbf{F}=m_i\ddot{x}_i-(\beta_{\mathrm{Lind}}+\beta_{\mathrm{Lang}})\dot{x}_i+\eta(t), \tag{3}$$

where $\eta(t)$ is a random force that serves to return the system to thermal equilibrium with the external reservoir.[33]

A recent implementation of a MD code optimized for ion-solid interaction studies employs the 256 processor CRI T3D MPP computer at LLNL. The implementation on the T3D of this code, MDCASK, is based on the PVM message passing library.[35] With these advances, on 128 processors the code runs at a rate of 2 μs/[atom (time step)] when using the SW potential, which has an interaction cutoff between the first- and second-nearest-neighbor shells, and a fourth-order predictor-corrector algorithm for integration of the equations of motion. That is, one MD iteration takes 2 s of CPU time for a crystal with 10^6 atoms.

III. MODIFIED STILLINGER-WEBER INTERATOMIC POTENTIAL

The simulation results presented in this paper were obtained with the Stillinger-Weber (SW) potential for silicon.[30] Although other potentials for silicon exist in the literature,[36] experience with the SW potential indicates that it is a reasonable representation of silicon for the study of ion-beam processing. This potential gives an accurate representation of many of the properties of bulk silicon, including a good description of its energy-volume relationship and of its melting behavior,[30] and of the recrystallization kinetics during fast quenching from the melt.[38] In addition, recent studies of the properties of silicon point defects and small clusters,[38,39] also support the validity claim for the SW potential. Comparison to very recent density functional calculations with *ab initio* pseudopotentials[40,41] shows good agreement between these electronic structure methods and the simple SW potential. For example, the SW potential predicts that the ⟨110⟩ split dumbbell configuration is the low-energy structure for the neutral self-interstitial.[38,39,42] This is in good agreement with first principles methods[40,41] although the exact details of the configuration may be slightly different.[39] The formation energy predicted is 3.65 eV for the SW potential[39] and 3.25 eV for the first principles methods.[41] On the other hand, the vacancy formation energy is about 1 eV lower (2.6 eV) for the SW potential[39] than the results of first principles calculations indicate.[41]

For the simulation of ion-beam processing the model interatomic potential has to be modified in the region of short interatomic separation. This is because many atoms interact at spacings well inside the core-core overlap region during the cascade process. This modification requires that some information regarding the form of the potential be known for distances of approach shorter than those characteristic of, for example, the pair distance in a ⟨110⟩ dumbbell. At sufficiently high energy, information on the core overlap region

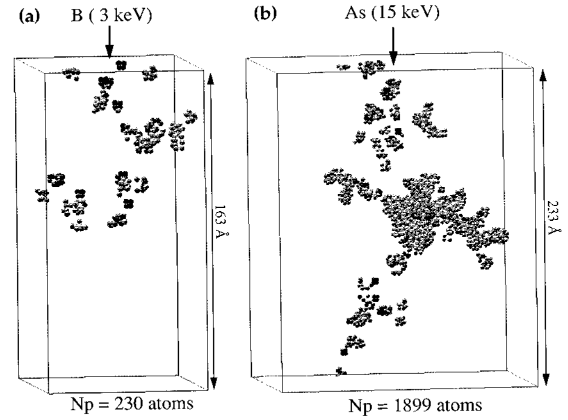

FIG. 1. Atoms with potential energy higher than 0.2 eV for 3 keV B (a) and 15 keV As (b) implantation in Si at 300 K after 10 ps.

of the potential exists from experiments of beam scattering in gases.[43] However, little or no direct information exists at intermediate energies, between ~20 eV and 500 eV. One piece of experimental data that can be used to explore the validity of the model potential in this intermediate-energy regime is the value of the threshold energy for defect production, E_d, along low-index crystallographic directions. In silicon, for example, the minimum value of E_d is known to be ~15–20 eV.[44] Recent simulations with the Tersoff potential gave minimum values of E_d~13 eV,[45] and those with the SW potential gave results for E_d of 18 eV along [111],[46] not far from the experimental values in either case. The SW results were also in agreement with experimental values of the orientation dependence of E_d.[46] These results indicate that these potentials are well suited to describe low-energy defect production mechanisms. Therefore, following the approach of Gärtner *et al.*,[47] we have modified the SW potential for distances of closest approach in a two-body collision shorter than those corresponding to threshold energy events. We spline the two-body part of the SW potential to the so-called universal or Biersack-Ziegler-Littmark (ZBL) potential.[48] The distances at which the two potentials are joined, as well as the form of the spline function, are given by Gärtner *et al.* in Ref. 47. We note here that the ZBL potential is a screened Coulomb interaction potential designed to describe properly the scattering properties of a very wide range of two-atom systems and is widely used in BCA codes such as the aforementioned MARLOWE and TRIM. In addition, we also use the ZBL potential to describe the interaction between the various energetic ions used in these simulations and the Si atoms. Because this is a pure repulsive interaction, no attempt is made to describe the equilibrium properties of the dopant-silicon pairs; rather we only describe the collisions among them.

IV. RESULTS

A. Ion mass and energy dependence of the as-implanted damage state in silicon

The primary damage state in a silicon crystal following 3 keV B and 15 keV As cascades is shown in Figs. 1(a) and 1(b), respectively. In units of reduced energy,[49] these PKA's

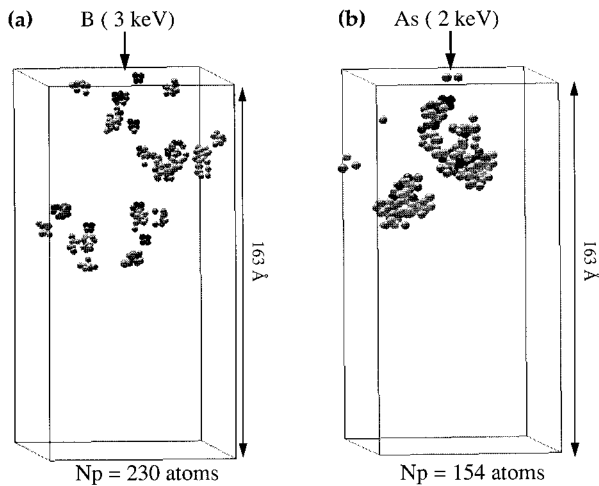

FIG. 2. Atoms with potential energy higher than 0.2 eV for 3 keV B (a) and 2 keV As (b) implantation in Si at 300 K after 10 ps.

TABLE I. Range, straggling, and damage energies as calculated with TRIM for several ions in silicon. ϵ is the reduced energy as defined by Lindhard.

Ion	Energy (keV)	Range (Å)	Straggling (Å)	Damage energy (keV)	ϵ[a]
B	1	49	22	0.4	0.11
B	2	83	37	0.8	0.23
B	3	130	70	1.3	0.34
As	2	36	11	1.3	0.01
As	5	64	20	3.4	0.02
As	10	100	32	7.2	0.05
As	15	125	45	10.8	0.07

[a]From Ref. 49.

correspond to 0.3 and 0.07. However, because of the different ion masses, the projected range of these PKA's is similar. Table I provides the projected range, straggling, and damage energy deposited, for each one of these cases as well as others discussed below, as obtained from TRIM.[21] Figure 1 shows the distribution of atoms with potential energy $E_p>0.2$ eV above the ground state of a silicon crystal 10 ps after the initiation of the PKA above the (001) surface plane. At this time, the energy deposited in the crystal by the PKA has been dissipated by the damped periodic boundaries. The gray scale represents atomic level stress σ, where $\sigma=\Omega^{-1}\delta(E_p)/\delta\xi$, Ω is the atomic volume of the crystal, and ξ is a distance scaling factor. Darker tones indicate tensile stress and lighter ones compressive stress. For the point defects, tensile stress indicates vacancies and compressive stress indicates interstitials. For example, four neighboring atoms under tensile stress in the figure correspond to an isolated vacancy. For the large clusters of disordered material, the average hydrostatic stress is nearly neutral.[27] The number of atoms, N_p, with $E_p>0.2$ eV is 230 and 1899 for the 3 keV B and the 15 keV As cases, respectively. Clearly seen in these figures is the fact that while 15 keV As cascades result in large clusters of these disordered atoms, both the number and size of the disordered atom clusters produced by the 3 keV B cascade are much smaller.

Also of interest is the comparison of different mass PKA's at the same damage energy, i.e., where the amount of energy deposited in elastic collisions is the same. Figure 2 shows two displacement cascades, one induced by a 3 keV B PKA (a) and the second by a 2 keV As PKA (b). In both these cases the damage energy is $E_D\sim 1.3$ keV.[21] It is interesting to note that despite the similar amount of damage energy deposited into the crystal, the morphology of the damage is substantially different in the two cases. In the As case, the damage distribution, as illustrated in Fig. 2 by the number of atoms with $E_p>0.2$ eV, is controlled by two large clusters and few isolated defects. However, in the case of the B implant, no large damage clusters appear and isolated vacancies, self-interstitials, and many small point defect clusters are visible.

Previously, we have shown that the disordered zones produced by 5 keV Si cascades in Si appear to be amorphous in nature.[27] This conclusion was based on analysis of the pair correlation function of the disordered zones and on the fact that solidification of the locally molten cascade zone occurs at a rate $\sim 10^{14}$–10^{15} K/s, which in Si leads to interface velocities much larger than the critical velocity for amorphization.[38] Here, we introduce a criterion based on the

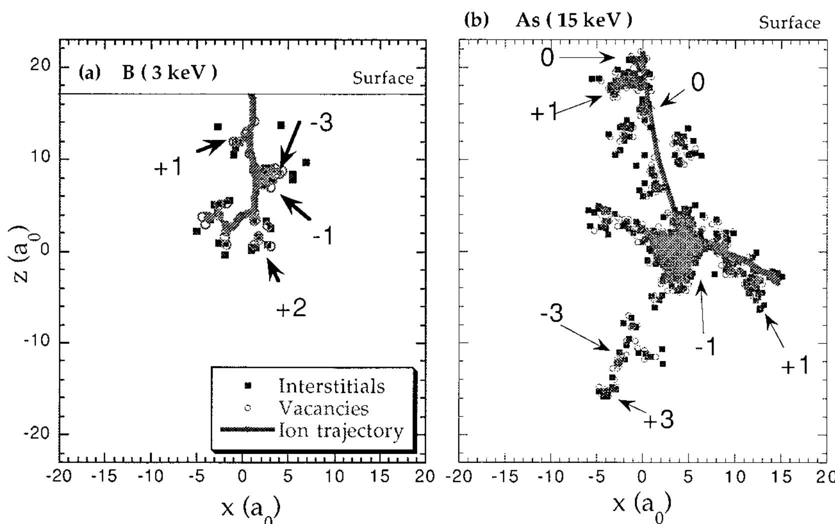

FIG. 3. 2D projection on a (010) plane of the V and I produced by 3 keV B (a) and 15 keV As (b) implantation in Si at 300 K after 10 ps.

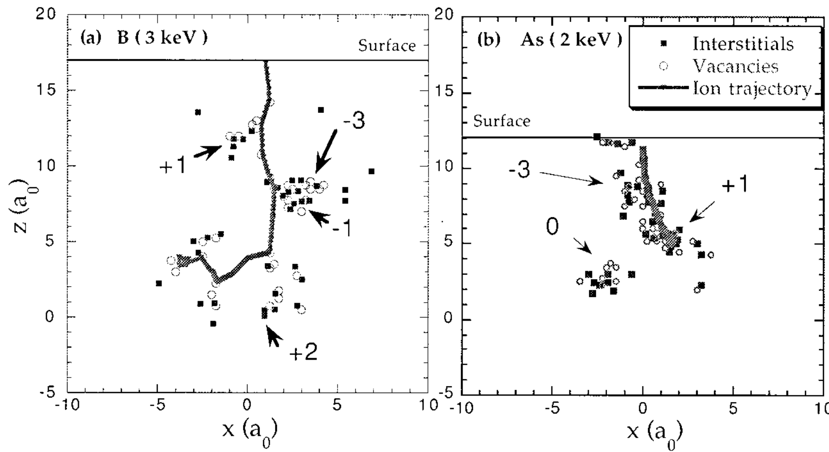

FIG. 4. 2D projection on a (010) plane of the V and I produced by 3 keV B (a) and 2 keV As (b) implantation in Si at 300 K after 10 ps.

time-averaged distribution of bond angles for the atoms in the cascade region. When performing a time average of the bond angle distribution subtended by an atom and its neighbors, the distribution becomes narrower for a crystalline sample, but remains invariant for an amorphous network. This difference in behavior allows the introduction of the following criterion: If after the time average a silicon atom is fourfold coordinated and the six possible angles that it forms with its neighbors fall within the limits of the averaged distribution during the same time for a perfect crystal, the atom is considered to be crystalline. Conversely, if this condition is not fulfilled, the atom is considered as part of an amorphous network. A more detailed description of the method and a comparison with criteria proposed by other authors is given elsewhere.[50] Applying this criterion to the center of a highly damaged region such as those shown in Fig. 1(b), we observe that 95% of the atoms are amorphous. Thus, we will refer to the large disordered zones, particularly those produced by high-mass ions such as As, as amorphous pockets throughout the rest of this paper.

Although a criterion based on the number of atoms with $E_p>0.2$ eV is useful to visualize and compare displacement cascades,[27] the underlying lattice may also be described in terms of the number of empty (vacancies) and multiply occupied (interstitials) lattice sites. An atom displaced from its original site more than the first-nearest-neighbor distance leaves behind a vacant site. This atom is then considered an interstitial if at the end of the cascade it is not within half the nearest-neighbor distance of a vacant site. If the atom stops at a lattice location within half the nearest-neighbor distance of a vacant site, it is then called a replacement, and there is no vacancy at the site. In most cases none of the atoms in the crystal are sputtered to form extra vacancies, and therefore the implanted ion creates one extra interstitial; i.e., $N_I=N_V+1$, where N_I is the final number of interstitials, and N_V is the final number of vacancies. Clearly, this definition of vacancies and interstitials is not physically appropriate in a highly disordered region such as the core of a displacement cascade where translational order has been lost.[27] Nevertheless, as we will discuss below, this definition is useful in describing the properties and nature of the damage and the way in which its stability affects damage accumulation and dynamic annealing at different temperatures.

Figure 3 shows a 2D projection on a (001) plane of the vacancies (V) and interstitials (I) produced by the 3 keV B (a) and 15 keV As (b) cascades of Fig. 1. Also indicated in the figure are the incoming ion and secondary recoil trajectories, and the excess (+) or deficit (−) of atoms in several of the damage clusters. The figure illustrates that while a number of isolated Frenkel (V-I) pairs and small clusters are observed in the case of the B cascade, large clusters of almost equal numbers of vacancies and interstitials dominate the damage in the As irradiation. Also, channeling of secondary recoils is illustrated by the fact that point defects and small clusters appear which are clearly disconnected from the bulk of the damage in Fig. 3(b). In Figs. 4(a) and 4(b) we show the 2D V-I plot for 2 keV As and 3 keV B cases, respectively. For these events the same damage energy is deposited in the crystal. The difference is striking in that many more isolated point defects are produced in the B case than in the As case.

In order to further quantify these observations, we plot in Fig. 5 the fraction of vacancies and interstitials in clusters smaller than size N versus the size of the cluster, for 2 keV

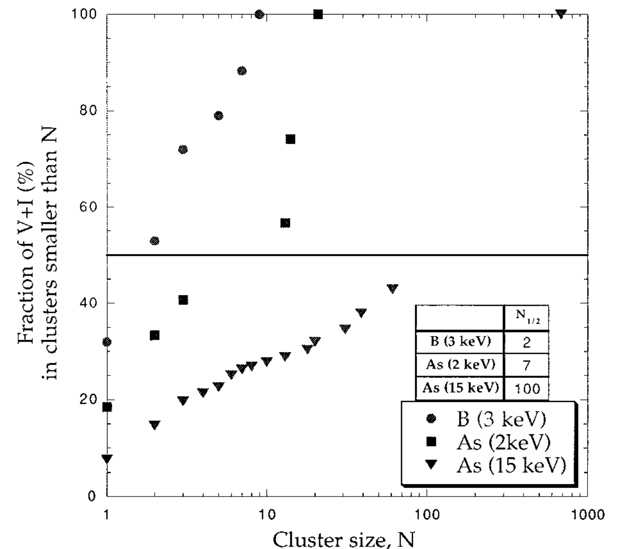

FIG. 5. Fraction of both V and I in clusters smaller than N, as a function of the cluster size (N), for different ion masses and energies.

TABLE II. Mean values of the number of atoms with $E_p>0.2$ eV ($\langle N_p\rangle$), number of interstitials and vacancies ($\langle N_{V+I}\rangle$), fraction of individual vacancies [$N_V(i)$], and interstitials [$N_I(i)$], maximum cluster size, and fraction of defects in clusters larger than 10. Results for different ions mass and energies on silicon at 300 K after 10 ps.

Ion	Energy (keV)	$\langle N_p\rangle$	$\langle N_{V+I}\rangle$	$N_V(i)$ (%)	$N_I(i)$ (%)	Maximum cluster size	Defects in clusters >10 (%)
B	1	73	28	22	27	9	8
B	2	182	61	29	31	8	13
B	3	235	76	33	40	12	10
As	2	273	144	7	15	63	72
As	5	652	376	7	8	225	73
As	10	1284	655	9	11	270	71
As	15	1729	1174	9	9	471	74

As, 3 keV B, and 15 keV As cascades. While the cluster distribution from the 3 keV B event is very narrow, with no clusters larger than 9 in this case, the 2-keV-As-induced cluster distribution is much broader, with a large cluster of 21 defects. Also interesting to note is the fact that for the 15 keV As case, which has the same projected range as the 3 keV B case (see Table I), the defect distribution is dominated by a large cluster with 685 defects. If we define as $N_{1/2}$ the 50% value of the cluster size distribution, then $N_{1/2}=2$ for 3 keV B, $N_{1/2}\sim 7$ for 2 keV As, and $N_{1/2}\sim 100$ for 15 keV As.

In Table II we present detailed results for 1, 2, and 3 keV B cascades and 2, 5, 10, and 15 keV As cascades. These numbers are averages over at least three independent events at each energy. The table provides the number of disordered atoms ($E_p>0.2$ eV), N_p, as well the total number of vacancies and interstitials, N_{V+I}, and the fraction of isolated vacancies and interstitials, $N_V(i)$ and $N_I(i)$. This last fraction is defined as those vacancies and interstitials which are at least 3.77 Å (the cutoff of the SW potential) away from another defect. The table quantifies the significant difference in the damage morphology between B and As cascades. While only about 10% of the vacancies and of the interstitials produced by the As cascades are isolated for $E>2$ keV, approximately 30% of vacancies and of interstitials are isolated for 2 and 3 keV B cascades. This fraction of isolated defects, which we refer to as the fraction of freely migrating, or mobile, defects, is important because it controls mass transport, at least at low temperatures where the large amorphous pockets are stable. Figures 3 and 4 clearly illustrate that for the same range or damage conditions the fraction of freely migrating defects with respect to the total number of defects produced by the ion increases as the mass of the ion decreases. Note also from Table II that the fraction of defects in clusters larger than 10 is about (8–13)% for B cascades, but ~70% for As cascades.

It is also of interest to analyze the way in which the damage distribution and morphology changes as the implantation energy increases. As the ion energy increases, not only does the total amount of damage increase, as expected, but the size of the largest amorphous pocket increases. This is also described in Table II where the last two columns give the size of the largest cluster, as well as the fraction of defects produced in clusters larger than 10. The presence of large clusters of defects indicates that for high-mass ions the damage morphology is governed by local melting in the cascade core which upon resolidification results in local amorphous pockets. Figure 6(a) shows the total number of interstitials, or displaced atoms, and the total number of isolated, mobile interstitials, as a function of recoil damage energy for As cascades. The total number of displaced atoms increases linearly with energy. As we will discuss in more detail below, the slope of this curve, $s_{\mathrm{As}}=55$ keV^{-1}, is approximately twice what would be predicted by BCA models, $s_{\mathrm{BCA}}=0.8/2E_d=27$ keV^{-1}, where $E_d=15$ eV is the threshold energy for defect production in Si. The fraction of mobile

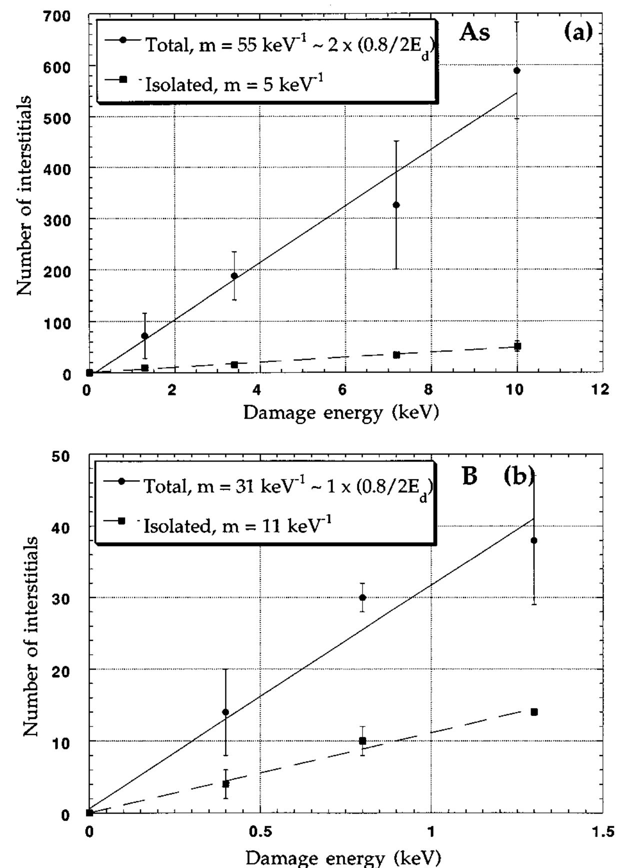

FIG. 6. Total number of displaced atoms and total number of mobile interstitials as a function of the damage energy for As (a) and B (b) implantations in silicon.

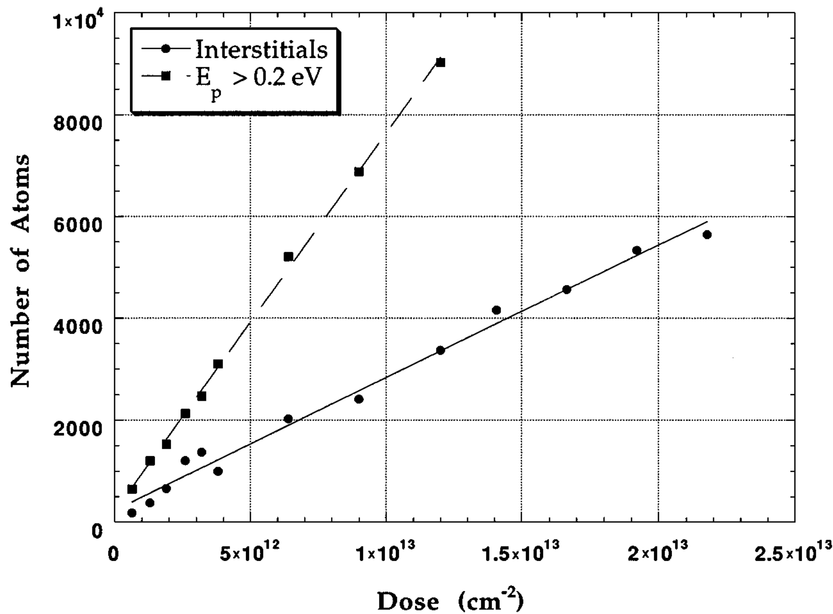

FIG. 7. Number of disordered atoms, $E_p > 0.2$ eV and number of interstitials as a function of the ion dose.

interstitials also increases with recoil energy, but with a different slope $s \sim 5$ keV^{-1}. For boron, Fig. 6(b) shows the displaced atoms and mobile defect production vs damage energy for 1, 2, and 3 keV displacement cascades. In contrast to the As case, the slope of the displacement production curve is $s_B = 31$ keV^{-1}, which is basically equal to the prediction of the BCA calculations. Also, the efficiency of mobile defect production for B cascades is 11 keV^{-1} in contrast to 5 keV^{-1} for the As results presented above.

Although the results discussed thus far have been obtained from a small number of individual displacement cascades at each energy, statistical variations can in principle play an important role in the interpretation of the data. In particular, when calculating the effect of channeling on the incoming ion range, accumulation of a large number of trajectories (~ 1000) is required.[51] This is clearly best achieved by BCA codes such as MARLOWE (Ref. 22) or Crystal-TRIM (Ref. 52) and is not attempted in this study. In addition, statistical variations on the shape of the cascade could lead to large variations in the number and configuration of displaced atoms. To test this effect, we plot in Fig. 7 the number of disordered atoms ($E_p > 0.2$ eV) and the number of interstitials versus the number of incoming PKA's (dose) for 5 keV As cascades in a silicon lattice at 80 K. Clearly, for the low doses accumulated in this study, the damage accumulation is linear. This is in excellent agreement with experimental evidence[53] and shows that when looking at average properties of cascades, statistical fluctuations play only a minor role.

B. Disordered zone stability and annealing kinetics

In order to understand damage accumulation and therefore the mechanisms of extended defect formation and amorphization, it is necessary to investigate in detail the stability of the amorphous pockets. At temperatures where point defects are not expected to be mobile (~ 80 K) in the time scale of an experiment, defect-defect interactions play a minor role. Direct amorphous pocket overlap should dominate the amorphization process, although some recrystallization of amorphous pockets due to local heating from neighboring cascades will occur. At higher temperatures the stability of the amorphous pockets and their interaction with mobile vacancies, interstitials, and possibly small clusters must be taken into account.

In the following, we discuss the temperature dependence of the annealing kinetics of amorphous pockets produced in silicon by 5 and 15 keV As cascades as well as 25 keV Pt implants. In a previous publication[27] we have shown that because of their large surface-to-volume ratio and the fact that they are surrounded by crystalline material, these amor-

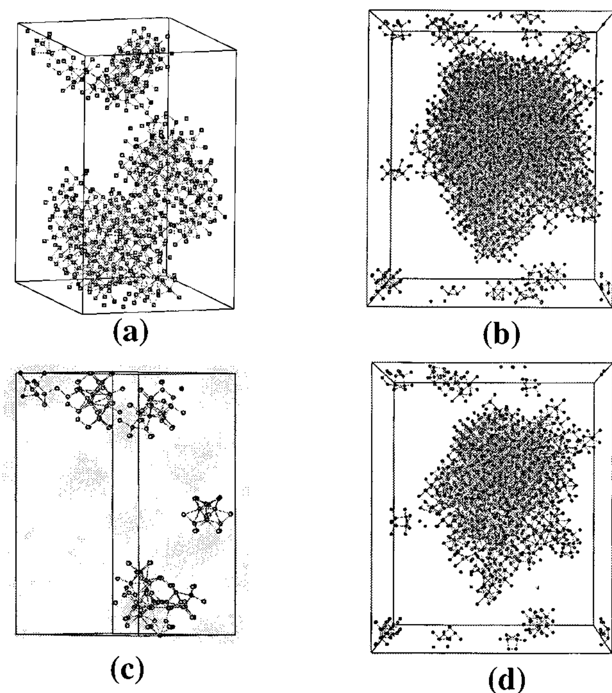

FIG. 8. Amorphous pocket produced by (a) 5 keV As implant and (b) 25 keV Pt implant. Anneal at 600 K for 0.5 ns of the pockets (c) 5 keV As and (d) 25 keV Pt.

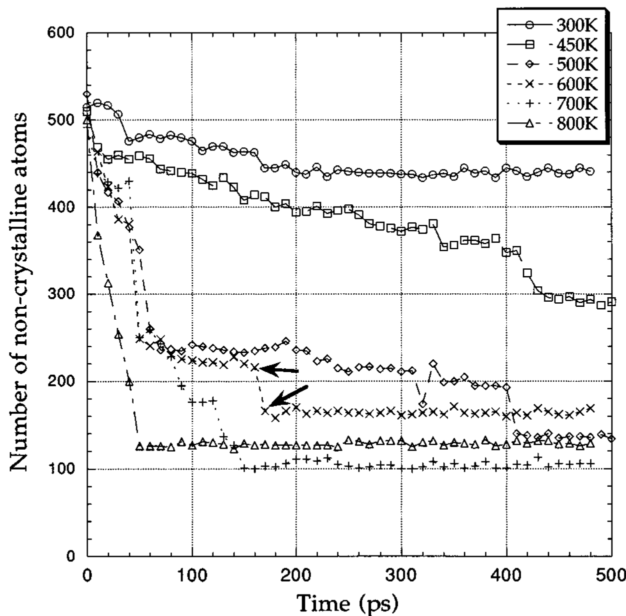

FIG. 9. Number of disordered atoms as a function of time for annealing at several temperatures of an amorphous pocket from a 5 keV As implant.

phous pockets are highly unstable and recrystallize at much lower temperatures than a stable planar amorphous/crystal (a-c) interface. This observation is in fact in very good agreement with experimental evidence.[54] In our previous work we also showed that upon annealing at sufficiently high temperature for 1 ns vacancies, interstitials and small point defect clusters appear in the recrystallized material.

In Fig. 8 we show amorphous pockets generated by (a) a 5 keV As and (b) a 25 keV Pt cascade in Si at room temperature. These pockets contain a total of 520 and 3975 noncrystalline atoms, respectively, where the criterion for defining these atoms has been given above. These pockets were annealed at various temperatures for times up to 0.5 ns. At 1080 K complete recrystallization of the damage has taken place by 0.1 ns, leaving behind point defects, in good agreement with our previous results. In Figs. 8(c) and 8(d) we present the atomic configurations of these pockets after 0.5 ns annealing at 600 K. Clearly, the smaller pocket belonging to the 5 keV As case has recovered to a much larger extent than has the 8 times larger pocket from the 25 keV Pt cascade.

The time evolution of the number of noncrystalline atoms for different annealing temperatures is shown in Fig. 9 for the amorphous pocket of Fig. 8(a). Note that at 300 K the pocket shrinks about 10% and then remains stable on this time scale, but that at 500 K a large fraction of the damage recovers and the pocket does not reach a stable configuration during the simulation. It is also interesting to note that for a planar (a-c) interface in silicon no motion occurs below 700 K,[55] so that these pockets are indeed less stable than the planar interface. Analysis of the pocket recrystallization kinetics in the early stages of the process can be done by considering the characteristic time τ required for the pocket to shrink to a specified fraction of its initial size $N_c = N_0/e$, with N_0 being the initial number of noncrystalline atoms in the pocket. From these numbers we calculate the average regrowth velocity for the different temperatures and obtain an *effective* activation energy. For three different pocket sizes, namely, $N_0 = 520$, 1550, and 3975 corresponding to 5 keV As, 15 keV As, and 25 keV Pt cascades, respectively, this *effective* activation energy has values of 0.23 eV, 0.37 eV, and 0.46 eV. Clearly, the recrystallization kinetics of these amorphous pockets depends strongly on the pocket size. The existence of such an effective activation energy is clearly related to the fact that we are not considering a planar a-c interface. We discuss this fact in more detail in the following section.

V. DISCUSSION

A. Total number of displaced atoms in silicon: Comparison to other models, experiments, and metal systems

The results presented in this paper provide quantitative information on the magnitude and state of clustering of the as-implanted damage produced under a wide variety of irradiation conditions in Si. At low temperature, the number of displacements can be estimated from the modified Kinchin-Pease expression of Sigmund[56] as $N_{k-p} = 0.8E_D/2E_d$, where E_D is the damage energy and E_d is the threshold energy for Frenkel pair production. As discussed in the Introduction, this expression is essentially based on the BCA and therefore gives roughly the same results as BCA-based computer codes such as TRIM and MARLOWE. In metal systems, it is well known that the efficiency of cascades for producing defects, $\zeta = N_{\mathrm{cas}}/N_{k-p}$, where N_{cas} is the actual number of defects produced in the cascade, decreases relative to the predictions of the BCA as the recoil energy increases.[57] In fact, ζ reaches a constant value of about 1/3 at high energies, where well-developed cascades appear.[57,58] This decrease in efficiency is a direct consequence of the local melting of the cascade core during the thermal spike.[59] Melting of the cascade absorbs many of the Frenkel pairs produced during the early collisional stages, in particular those where the vacancy-interstitial (V-I) pair is not well separated by either long replacement collision sequences (RCS's) or high-energy ballistic events. Later on, resolidification of the low-density melt during cascade cooling leads to the freezing-in of a few defects, but in metals does not result in local amorphization.[59] The final number of defects after the thermal spike is thus reduced relative to the production during the early collisional stages and, therefore, relative to the BCA predictions. In the simulations of Si presented here, the displacement production in cascades is much different from that observed in metals. As we have discussed previously, the small number of isolated Frenkel pairs produced directly in cascades in Si is related to the short length of RCS's.[27] Also, we have shown in Fig. 6 that the number of displaced atoms increases with recoil damage energy with a slope that is twice as large as the modified Kinchin-Pease expression for high-mass ions and at the same rate for low-mass ions. In Si, local melting of the cascade core results in amorphous pockets, and these contain many more displaced atoms than just simply those produced directly in high-energy binary collisions. For low-mass ions, where local melting in the cascade does not take place, defect production is essentially governed by the early collisional phase of the cascade and therefore agrees well with the BCA predictions.

The results of the MD simulations presented here are consistent with the experimental observations of Schreutelkampf *et al.*[60] These authors used Rutherford backscattering spectroscopy (RBS) and channeling experiments to extract the number of Si atoms displaced off lattice sites at room temperature for a wide variety of irradiation conditions. Their results show that for very-high-mass ions such as In and Sb, the observed number of Si atoms displaced off lattice sites $[\mathrm{Si}_d(\mathrm{RBS})]$ is always larger than the TRIM prediction $[\mathrm{Si}_d(\mathrm{TRIM})]$. In addition, they also observed that for an intermediate mass ion such as Ga, $\mathrm{Si}_d(\mathrm{RBS}) > \mathrm{Si}_d(\mathrm{TRIM})$ at low energy where the defects are mainly produced in cascades, but $\mathrm{Si}_d(\mathrm{RBS}) < \mathrm{Si}_d(\mathrm{TRIM})$ at 1 MeV where defect production is dominated by low-energy recoil events that lead to isolated Frenkel pairs. For low-energy ions such as B, $\mathrm{Si}_d(\mathrm{RBS})$ was always smaller than $\mathrm{Si}_d(\mathrm{TRIM})$, as opposed to the results of our MD simulations where the number of displaced atoms for B cascades is similar to the TRIM predictions. This difference is in fact not unreasonable and can be understood by considering again the actual morphology of the damage. As we have seen in Table II, a large fraction of the displaced atoms ($\sim 30\%$) for low-mass ions such as B are in the form of isolated vacancies and interstitials, which in Si are known to be mobile at room temperature.[61] Thus, the as-produced displacement field will be reduced in magnitude over long times even at room temperature through bulk recombination and annihilation at surfaces and internal sinks. This effect is clearly stronger for low-mass ions, so that we expect our results to be quantitatively more accurate for heavier ions such as As where very few isolated, mobile point defects are produced in the cascades.

Larsen *et al.*[61] have unequivocally shown that at room temperature there exists a population of mobile defects which is able to escape the cascade region and migrate at room temperature. These defects were detected by their ability to induce changes in dopant activation well inside the bulk, away from the implanted region. It was shown that the number of injected defects increases as the ion mass increases, considering the same projected range of the ions. This result is consistent with our calculations. From Table II, the fraction of freely migrating defects for B is 30%, therefore, only ≈ 20 free defects for a 3 keV B implant, while for 15 keV As, which has the same projected range, there are ≈ 100 freely migrating defects, according to our results. However, the fraction of freely migrating defects with respect to the total number of defects produced is 30% for B and 9% for As. This is also consistent with the results from Larsen *et al.* where they find that the defect injection efficiency into the bulk is 40% lower for Pt than for Si ions. Our results confirm the interpretation of Larsen *et al.* that the reduction in the injection efficiency for heavy ions is due to the fact that a large fraction of generated defects collapse into amorphous clusters in the cascade.

B. Recrystallization kinetics of amorphous pockets

The kinetics of recrystallization of a planar *a-c* interface has been studied extensively, as indicated by theoretical[62,63] and experimental publications.[55,64–66] A single activation energy for thermal recrystallization of such an interface with a value of ~ 2.68 eV (Ref. 65) has been found, therefore suggesting a single mechanism for recrystallization. The most accepted model explaining this phenomenon was originally proposed by Spaepen and Turnbull[62] and later extended by Lu *et al.*[63] According to this model, recrystallization takes place by generation of dangling bonds at the *a-c* interface that migrate and induce reordering. The experimental activation energy could be explained as the combination of the energy of formation of a dangling bond, 2.246 eV in Si, and a migration energy of ~ 0.43 eV.[63]

The situation we consider in this work is different in the sense that we are not dealing with planar *a-c* interfaces but rather inhomogeneous shapes. The curves in Fig. 9 show plateaus during recrystallization where almost no change in the number of disordered atoms occurs and step regions where a high number of atoms recrystallize in a very short time. Also clearly seen in the figure is the fact that the time between the steps and the plateaus decreases as the annealing temperature increases. The evolution of the noncrystalline atoms as a function of time is a rather more complicated process than a simple exponential decay and makes the analysis of the amorphous zone stability in terms of a simple activation energy very difficult. The effective activation energies for regrowth quoted in Sec. IV B are much lower that that observed experimentally for solid phase epitaxy (SPE) of planar amorphous-crystalline silicon interfaces, and in fact are closer to values related to the migration of dangling bonds, therefore revealing that the formation of such type of defects may not be necessary, at least for small pockets. The irregular shape of the pockets already provides the necessary sites for recrystallization, as postulated by Priolo *et al.*[66]

Detailed analysis of the atomic configurations indicates that the recrystallization behavior is very likely related to a process or reordering of atoms at the amorphous-crystal interface. According to the model proposed by Spaepen[67] an *a-c* interface is formed by planar (111) faces connected to a random network. Williams and Elliman[68] proposed that the dangling bonds responsible for the recrystallization are in fact located at kink sites on [110] ledges separating the (111) terraces. The recrystallization will occur along the [110] ledges once a kink is formed. Considering this model, the plateaus observed in Fig. 10 could be related to the formation of kink sites. Once they are formed, recrystallization of several atoms will occur in a very short time. We have studied in detail the evolution of the region of the *a-c* interface where recrystallization occurs for the step identified by the arrow during the 600 K anneal in Fig. 9. In Fig. 10 we show how this region, which is where the recrystallization occurs, changes in going from 160 to 170 ps. The dark atoms correspond to crystalline atoms and the lighter ones are amor-

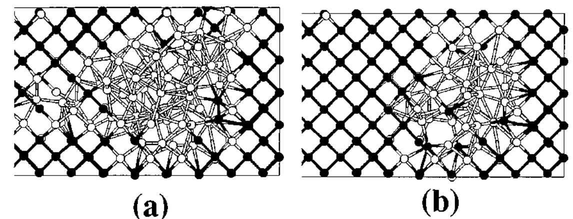

FIG. 10. Configuration of an amorphous pocket from a 5 keV As implant. Annealing during 160 ps (a) and 170 ps (b) at 600 K. These configurations correspond to the step marked as (a) and (b).

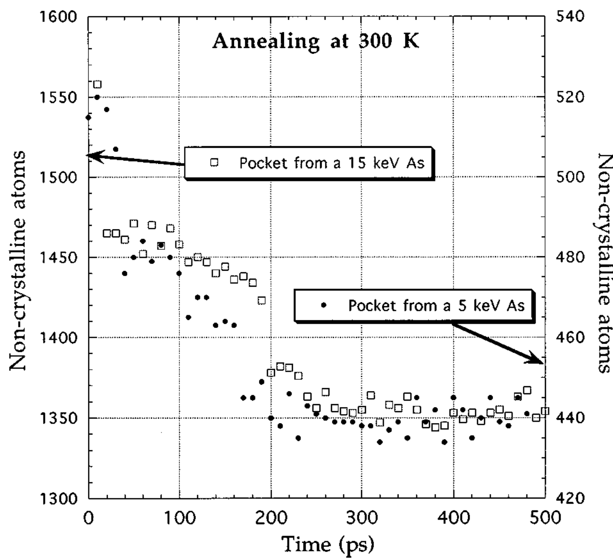

FIG. 11. Number of noncrystalline atoms as a function of annealing time at 300 K for 5 keV As implant and 15 keV As implant.

phous, according to the criterion already described above. Observe that most of the recrystallization has occurred in the same side of the pocket (although some changes occur at the interface), producing a total of 50 atoms that change from belonging to the amorphous network to crystal in just 10 ps. This corresponds to approximately 0.5 atoms per lattice vibration period, indicating that the regrowth in this case is not related to a simple defect diffusion process. Clearly, as we can see in Fig. 9, the time for a step to occur increases as the annealing temperature decreases, reenforcing the idea of defect nucleation at the interface.

One of the interesting observations from these results is that recrystallization of the amorphous pockets occurs without the intervention of point defects external to the pocket. In particular, divacancies do not play a role in the pocket recrystallization process, therefore eliminating a possible vacancy diffusion recrystallization mechanism. Models based on diffusion of defects in the bulk of the amorphous phase to the interface have also been proposed to explain recrystallization in an *a*-*c* planar interface.[69] Experimentally, the lack of a recrystallization rate dependence on amorphous layer thickness rules out these models.[63] In our results, at temperatures below about 600 K the velocity of regrowth decreases as the size of the pocket increases. In contrast, in a diffusion model a larger amorphous pocket would contain a higher density of defects in the bulk and therefore the crystallization velocity should increase. This fact together with the structure analysis of Fig. 12 and the presence of plateaus and steps in the time evolution of the damage, Fig. 10, seems to indicate that the process is governed by interface reactions and not defect production and diffusion in the bulk of either the amorphous pocket or the crystal.

One of the important questions that must be answered to understand ion-beam-induced amorphization is what is the range of stability of the amorphous pockets at room and intermediate temperatures. From Fig. 9 we can see that at room temperature there is a small decrease on the number of amorphous atoms during the first 0.2 ns related to the relaxation of some atoms surrounding point defects in the damage cluster. Afterwards, N_a remains constant up to 0.5 ns, although it is possible that further annealing could occur for longer times, even at room temperature (RT). We can estimate the amorphous pocket annealing rate at 300 K using the *effective* activation energies obtained above for different pocket sizes at higher temperatures. In the case of 520, 1550, and 3975 atoms, those times are 0.013, 0.5, and 10 μs, respectively. These results are obtained assuming that there is an exponential decay in the number of atoms that recrystallize at RT. However, as we already pointed out above, the curves in Fig. 9 can not be fitted to a single exponential. In Fig. 11 we show the annealing at 300 K of the pockets produced by 5 keV and 15 keV As implants. The initial recovery is fast, with many atoms recrystallizing. However, the process stabilizes after ~200 ps and the number of atoms in a noncrystalline state remains stable for both pockets. Following the models of Spaepen and Turnbull[62] and Priolo *et al.*,[66] this stability would set in when all the available sites for recrystallization have been filled. The possibility of a new site would require the formation of a dangling bond at the interface, with an activation energy of 2.23 eV and, con-

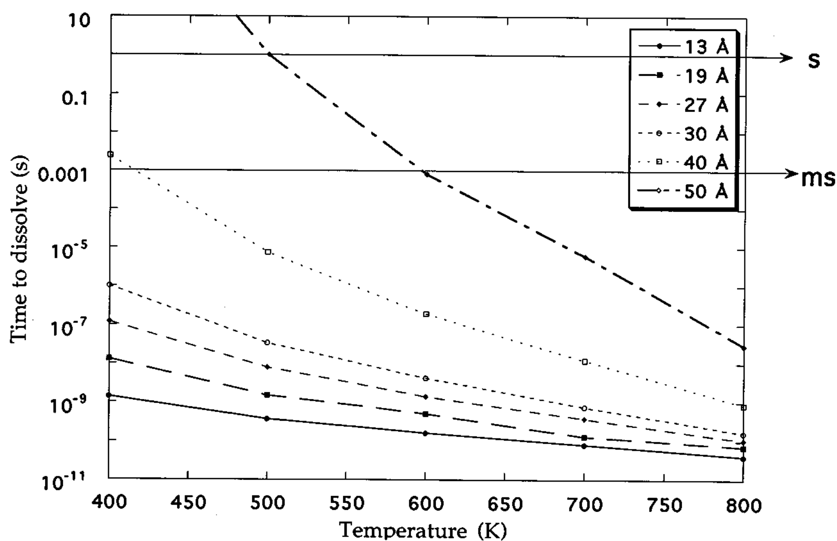

FIG. 12. Time to dissolve an amorphous pocket as a function of the temperature for different pocket sizes.

sequently, a time of the order of 3.4×10^{13} s for a 300 K anneal. Therefore, at room temperature the damage produced by heavy ions remains stable at least for energies higher than 5 keV, which are the lowest considered in this work.

There is extensive experimental evidence for the existence of large disordered zones resulting from ion implantation at low doses that are stable at room temperature. Ruault *et al.*[70] studied the stability of amorphous pockets produced by 50 and 200 keV Bi implants in silicon in transmission electron microscopy (TEM) and concluded that these regions are essentially stable at room temperature or below. Similar results have been obtained by numerous other authors.[54,71]

C. Role of the as-implanted damage state on the dynamics of amorphization

The large fraction of defects in clusters and amorphous zones as a result of intermediate- and high-mass ion irradiation of silicon has important consequences. This implies that the damage annealing kinetics is complex and not simply dependent on point defect mobilities and interstitial-vacancy recombination. Our results have shown that at low temperature the main contribution to amorphization of Si arises from the fraction of defects produced in clusters or amorphous pockets. If amorphization were caused by point defect accumulation alone, the critical dose for amorphization would be lower for lower-mass ions of the same damage energy since more isolated Frenkel pairs are produced in this case. This is contrary to experimental observation.[72] For heavy ions where large amorphous pockets are produced, the damage stability results described in the previous section appear to indicate that no dose rate dependence of amorphization should exist for irradiation of silicon at temperatures at or below room temperature. However, at or above a certain temperature (which depends on the original pocket size and thus on the damage energy of the ion) the amorphous pockets produced by the cascades recrystallize, leaving populations of point defects and small clusters. Therefore, one would expect a critical temperature, given by the temperature at which the amorphous pockets dissolve, above which no heterogeneous amorphization of silicon is possible by ion irradiation, although homogeneous amorphization by the accumulation of point defects could take place. If we consider that amorphous pocket stability is higher the larger the pocket size, and that the fraction of displacements initially in the form of amorphous pockets increases with ion mass, this critical temperature should then clearly increase with ion mass.

Considering the activation energies obtained for the different pockets in this study we can estimate the time required to dissolve a pocket depending on its initial size and the irradiation temperature. We present the results of this calculation in Fig. 12 where we plot the time required for a pocket dissolution versus temperature for a variety of pocket sizes. The graph considers only irradiation temperatures above 600 K where we have seen that the amorphous pockets are not stable and do indeed dissolve over time. For dose rates between 10^{12} and 10^{14} ions/(cm^2 s), which correspond to cascade overlap times of approximately 1 s and 10 ms, respectively, we can conclude from Fig. 12 that heterogeneous amorphization at temperatures at and above 600 K can only occur for cascades of size larger than 50 Å in radius. For smaller cascade sizes, the time scale for amorphous pocket annealing ($\sim$0.1–0.5 ns) is much shorter than the time between cascade overlaps, which for the highest ion flux used in experiments is only of the order of milliseconds. Therefore, we would expect no heterogeneous amorphization to occur for almost any irradiation condition at temperatures above 600 K. These results are consistent with the experiments of Elliman *et al.*[3] who have shown that amorphization is not possible with 1.5 MeV Xe ions above 600 K at any experimentally accessible dose rate. This is also consistent with the experiments of Vook[2] who have shown that the critical dose for amorphization diverges above 500 K for ions as heavy as Sb.

VI. CONCLUSIONS

The simulations presented in this paper provide quantitative information, at the atomic level, on the nature of implantation damage in Si under a wide variety of conditions. The results show that the morphology of the as-implanted damage is strongly dependent on the mass of the ion. A large number of isolated Frenkel pairs are formed for light-ion irradiation such as B, more than twice the number formed by As ions with the same damage energy. On the other hand, the number of displaced atoms is larger for the As ions, with the damage mostly in the form of large defect clusters and amorphous pockets. For light ions, the predictions of codes based on the BCA regarding the total number of displaced atoms are accurate; most displaced atoms are produced during the early ballistic phase of the cascade. However, for heavy ions such as As, intracascade amorphization results in large damage volumes per cascade, and therefore in more displaced atoms than those predicted by the BCA. This effect is the result of the dense cascade regions that are produced by the heavy ions. The deposition of a large amount of kinetic energy in a small region of the crystal increases the efficiency of the displacement process. The energy per atom required to melt the material in the region of the cascade is much smaller than the threshold energy to form a Frenkel pair. The cooperative displacement of a group of atoms in a process similar to melting accounts for the large number of atoms displaced in the cascade regions.

The stability of the damage zones at the ambient temperature and during annealing has important implications for ion-induced amorphization and for the diffusion of dopants during the processing of devices. We have shown that damage created by 5 keV As irradiation can be mostly eliminated by short, high-temperature anneals, e.g., a temperature of 1080 K for only 150 ps. The damage microstructure following this anneal has the form of point defects and small clusters of vacancies or interstitials left behind when the amorphous region recrystallizes. In most cases the amorphous zones have an excess or deficit of atoms compared with the surrounding perfect crystal, and recrystallization simply leaves the corresponding number of vacancies or interstitials in a small cluster.

We have also investigated the annealing at different temperatures of an amorphous pocket produced by a 5 keV As ion. Even at room temperature, the number of atoms in the amorphous zone decreases by over 10% in a period of 0.5 ns, but after that it appears to be stable over very long time scales. At higher annealing temperatures the size of the zone

decreases by a larger amount, and at 800 K only about 20% of the atoms remained in an amorphous configuration. This shows that the material in a single amorphous zone can have different levels of metastability against recrystallization.

The influence of the size of the amorphous zone on recrystallization has been studied by annealing pockets of different sizes at different temperatures. The larger pockets clearly have greater metastability against recrystallization, as indicated by a higher apparent activation energy. Amorphization by the accumulation of amorphous zones would require that a zone remain until other cascades are generated in its vicinity. Since the time for overlap of cascades is on the order of 0.01–1.0 s for dose rates in the range of 10^{14}–10^{12} ions/(cm^2 s), the zones would be required to be stable for times much longer than those that can be simulated by MD. However, extrapolation of the simulation results to larger amorphous pockets than the ones simulated in this work indicates that an heterogeneous amorphization process at temperatures higher than 600 K would require amorphous zones of a radius of about 50 Å. Since the size of these amorphous pockets is strongly dependent on the ion mass, and the stability of the amorphous pockets increases with size, the critical temperature required to eliminate amorphization will increase as the ion mass increases. These observations are in very good agreement with the experimental database.

We have shown that it is possible to obtain accurate data on the amount of damage produced by ion-beam irradiation by simulating a modest number of events. Although the range of individual ions varies considerably, requiring the simulation of thousands of events by TRIM or MARLOWE in order to obtain accurate statistics, the total amount of damage produced is not subject to such large fluctuations. The detailed collisions experienced by an ion can have a large effect on the range, but they do not have a large effect on the total damage, which involves a much larger number of energetic particles. A particularly hard collision with a silicon atom near the surface may drastically affect the distance the ion moves into the crystal, while the total number of atoms that experience large displacements is not much affected. This has been proved by BCA models,[22] where it is observed that the displacement efficiency has a small dependence on parameters like the inelastic energy loss model considered, the temperature of the target, or the cutoff energy for the projectile. We have found that good damage statistics can be achieved using fewer than 100 events, and for this reason the MD method is well suited to this type of study.

In order to develop more general models of damage accumulation and annealing, more accurate and physically correct models based on MD predictions for the damage will be required. This paper provides the underlying base required to develop such models. Based on the results of amorphous pocket annealing, we are currently developing a hybrid approach that uses both MD and kinetic Monte Carlo simulations to study damage accumulation at different temperatures. These results will then be used to study amorphization, damage annealing, and TED under a wide variety of irradiation masses and energies.[73,74]

ACKNOWLEDGMENTS

This work was performed under the auspices of the U.S. Department of Energy by Lawrence Livermore National Laboratory under Contract No. W-7405-Eng-48 and by Bell Laboratories. The authors are grateful to S. Coffa and F. Priolo for helpful discussions. One of us (M.J.C.) thanks the Juan Gil Albert Association of Alacant and the Spanish DGICYT (Project No. PB92-0341) for partial support.

*Permanent address: Department de Física Aplicada, Universitat d'Alacant, Spain.

†Permanent address: Department de E. y Electronica, Universidad de Valladolid, Spain.

[1] J.S. Williams, Mater. Res. Soc. Bull. **17**, 47 (1992).

[2] F.L. Vook, in *Radiation Damage and Defects in Semiconductors*, edited by J.E. Whitehouse (The Institute of Physics, London, 1973), p. 60.

[3] R.G. Elliman, J. Linros, and W.L. Brown, in *Fundamentals of Beam-Solid Interactions and Transient Thermal Processing*, edited by M. J. Aziz *et al.*, MRS Symposia Proceedings No. 100 (Materials Research Society, Pittsburgh, 1988), p. 363.

[4] P. J. Schultz, C. Jagadish, M.C. Ridgeway, R.G. Elliman, and J.S. Williams, Phys. Rev. B **44**, 9118 (1991).

[5] R.D. Goldberg, R.G. Elliman, and J.S. Williams, Nucl. Instrum. Methods B **80/81**, 596 (1993).

[6] T. Motooka and O.W. Holland, Appl. Phys. Lett. **61**, 3005 (1992).

[7] T. Motooka and O.W. Holland, Appl. Phys. Lett. **58**, 2360 (1991).

[8] See, e.g., *Handbook of Ion Implantation*, edited by J.F. Ziegler (North-Holland, Amsterdam, 1992).

[9] K.S. Jones, H.G. Robinson, J. Listebarger, J. Chen, J. Liu, B. Herner, H. Park, M.E. Law, D. Sieloff, and J.A. Slinkman, Nucl. Instrum. Methods B **96**, 196 (1995).

[10] D.J. Eaglesham, P.A. Stolk, H.-J. Gossman, and J.M. Poate, Appl. Phys. Lett. **65**, 2305 (1994).

[11] P.A. Stolk, H.J. Gossmann, D.J. Eaglesham, and J.M. Poate, Nucl. Instrum. Methods B **96**, 187 (1995).

[12] W.K. Hofer, H.W. Werner, D.P. Oosthoek, and N.J. Koeman, Appl. Phys. Lett. **4**, 125 (1974).

[13] W. Taylor, B.P.R. Marioton, T.Y. Tan, and U. Gossele, Radiat. Eff. Defects Solids **111/112**, 131 (1989).

[14] A.E. Mitchel, Nucl. Instrum. Methods B **37/38**, 379 (1989).

[15] N.E.B. Cowern, K.T.F. Janssen, and H.F.F. Jos, J. Appl. Phys. **68**, 6191 (1990).

[16] M.D. Giles, J. Electrochem. Soc. **138**, 1160 (1991).

[17] *The National Technology Roadmap for Semiconductors* (Semiconductor Industry Association, San José, 1994).

[18] M.L. Swanson, J.R. Parsons, and C.W. Hoelke, Radiat. Eff. **9**, 249 (1971).

[19] F.W. Morehead and B.L. Crowder, Radiat. Eff. **6**, 27 (1970).

[20] S.J. Zinkle and B.N. Singh, J. Nucl. Mater. **199**, 173 (1993).

[21] J.F. Ziegler, *Stopping and Ranges of Ions in Matter* (Pergamon, New York, 1977), Vol. 1.

[22] M.T. Robinson and I.M. Torrens, Phys. Rev. B **9**, 5008 (1974).

[23] K.B. Winterbon, P. Sigmund, and J.B. Sanders, K. Dan. Vidensk. Selsk. Mat. Fys. Medd. **37**, 14 (1970).

[24] P. Sigmund, Rev. Roum, Phys. **17**, 823 (1972).

[25] M. Jaraíz, G.H Gilmer, and T. Díaz de la Rubia, Appl. Phys. Lett. **68**, 409 (1996).

[26] J.B. Gibson, A.N. Goland, M. Milgram, G.H. Vineyard, Phys. Rev. **120**, 1229 (1960).
[27] T. Díaz de la Rubia and G.H. Gilmer, Phys. Rev. Lett. **74**, 2507 (1995).
[28] D.J. Bacon, A.F. Calder, F. Gao, V.G. Kapinos, and S.J. Wooding, Nucl. Instrum. Methods B **102**, 37 (1995).
[29] M.P. Allen and D.J. Tildesley, *Computer Simulation of Liquids* (Oxford Science, New York, 1987).
[30] F.H. Stillinger and T.A. Weber, Phys. Rev. B **31**, 5262 (1985).
[31] J.R. Beeler, Jr., *Computer Simulation in Materials Science* (ASM International, New York, 1988), p. 45.
[32] W.E. King and R. Benedek, J. Nucl. Mater. **117**, 26 (1983).
[33] D.W. Heermann, *Computer Simulation Methods in Theoretical Physics* (Springer-Verlag, Berlin, 1986).
[34] J. Lindhard and M. Scharff, Phys. Rev. **124**, 128 (1961).
[35] PVM3 Users Guide and Reference Manual [Oak Ridge National Laboratory Report No. ORNL/TM-12187, 1993 (unpublished)].
[36] J. Tersoff, Phys. Rev. B **39**, 5566 (1989).
[37] M.H. Grabow, G.H. Gilmer, and A.F. Baker, in *Atomic Scale Calculations in Materials Science*, edited by J. Tersoff *et al.*, MRS Symposia Proceedings No. 141 (Materials Research Society, Pittsburgh, 1989), p. 349.
[38] R.A. Brown, D. Maroudas, and T. Sinno, J. Cryst. Growth **137**, 12 (1994).
[39] G.H. Gilmer, T. Diaz de la Rubia, M. Jaraiz, and D. Stock, Nucl. Instrum. Methods B **102**, 247 (1995).
[40] P.E. Blochl, E. Smargiassi, R. Car, D.B. Laks, and S.T. Pantelides, Phys. Rev. Lett. **70**, 2435 (1993).
[41] J. Zhu, L. Yang, C. Mailhiot, T. Diaz de la Rubia, and G.H. Gilmer, Nucl. Instrum. Methods B **102**, 29 (1995).
[42] H.R. Schober, Phys. Rev. B **39**, 13 013 (1989).
[43] I.M. Torrens, *Interatomic Potentials* (Academic Press, New York, 1972).
[44] J.W. Corbett, *Solid State Physics* (Academic Press, New York, 1966), Vol. 7.
[45] L.A. Miller, D.K. Brice, A.K. Prinja, and S.T. Picraux, Radiat. Eff. Solids **129**, 127 (1994).
[46] M.J. Caturla, T. Diaz de la Rubia, and G.H. Gilmer, in *Materials Synthesis and Processing Using Ion Beams,* edited by R.J. Culbertson *et al.*, MRS Symposia Proceedings No. 316 (Materials Research Society, Pittsburgh, 1994), p. 111.
[47] K. Gärtner, D. Stock, B. Weber, G. Betz, M. Hautala, G. Hobler, M. Hou, S. Sarite, W. Eckstein, J.J. Jiménez-Rodríguez, A.M.C. Pérez-Martín, E.P. Andribet, V. Konoplev, A. Gras-Martí, M. Posselt, M.H. Shapiro, T.A. Tombrello, H.M. Urbassek, H. Hensel, Y. Yamamura, and W. Takeuchi, Nucl. Instrum. Methods B **102**, 183 (1995).
[48] J.F. Ziegler, J.P. Biersack, and U. Littmark, *The Stopping and Range of Ions in Solids,* Vol. 1 of *The Stopping and Range of Ions in Matter*, edited by J.F. Ziegler (Pergamon, New York, 1985), p. 25ff.
[49] J. Lindhard, M. Scharff, and H.E. Schiøtt, K. Dan. Vidensk. Selsk. Mat. Fys. Medd. **33**, 14 (1963).
[50] L.A. Marqués, M.-J. Caturla, and T. Diaz de la Rubia, J. Appl. Phys. (to be published).
[51] K.M. Klein, C. Park, and Al F. Tasch, IEEE Trans. Electron. Devices **ED-39**, 17 (1992).
[52] M. Posselt, Nucl. Instrum. Methods B **96**, 163 (1995).
[53] G. Bai and M.-A. Nicolet, J. Appl. Phys. **70**, 649 (1991).
[54] L.M. Howe and M.H. Rainville, Nucl. Instrum. Methods **182/183**, 143 (1981).
[55] R.G. Elliman, J.S. Williams, W.L. Brown, A. Leiberich, D.M. Maher, and R.V. Knoell, Nucl. Instrum. Methods B **19/20**, 435 (1987).
[56] P. Sigmund, Appl. Phys. Lett. **14**, 114 (1969).
[57] R.S. Averback, R. Benedek, and K.L. Merkle, Phys. Rev. B **18**, 4156 (1978).
[58] M.W. Guinan and J.H. Kinney, J. Nucl. Mater. **103/104**, 1319 (1981).
[59] T. Díaz de la Rubia, R.S. Averback, R. Benedek, and W.E. King, Phys. Rev. Lett. **59**, 1930 (1987).
[60] R.J. Schreutelkamp, J.S. Custer, J.R. Liefting, W.X. Lu, and F.W. Saris, Mater. Sci. Rep. **6**, 1 (1991).
[61] K.K. Larsen, V. Privitera, S. Coffa, F. Priolo, S.U. Campisano, and A. Carnera, Phys. Rev. Lett. **76**, 1493 (1996).
[62] F. Spaepen and D. Turnbull, in *Laser Solid Interactions and Laser Processing*, edited by S.D. Ferris, H.J. Leamy, and J.M. Poate (Materials Research Society, Boston, 1978).
[63] G.-W. Lu, E. Nygren, and M.J. Aziz, J. Appl. Phys. **70**, 5323 (1991).
[64] E. Rimini, *Ion Implantation: Basics to Device Fabrication* (Kluwer Academic Publishers, Boston, 1995).
[65] L. Csepregi, E.F. Kennedy, J.W. Mayer, and T.W. Sigmon, J. Appl. Phys. **49**, 3906 (1978).
[66] F. Priolo, A. Battaglia, and R. Nicotra, Appl. Phys. Lett. **57**, 768 (1990).
[67] F. Spaepen, Acta Metall. **26**, 1167 (1978).
[68] J.S. Williams and R.G. Elliman, Phys. Rev. Lett. **51**, 1069 (1983).
[69] J. Narayan, J. Appl. Phys. **53**, 8607 (1982).
[70] M.O. Ruault, J. Chaumont, J.M. Penisson, and A. Borret, Philos. Mag. A **50**, 667 (1984).
[71] J. Narayan, O.S. Oen, D. Fathy, and O.W. Holland, Mater. Lett. **3**, 67 (1985).
[72] T. Motooka and O.W. Holland, Appl. Phys. Lett. **61**, 3005 (1992).